Study on Electromechanical Coupling Characteristics of an Integrated Electric Drive System for Electric Vehicle

JIANJUN HU[1,2], **TAO PENG**[2], **MEIXIA JIA**[2], **YING YANG**[2], **AND YONGJIE GUAN**[2]
[1]State Key Laboratory of Mechanical Transmission, Chongqing University, Chongqing 400044, China
[2]Department of Automotive Engineering, Chongqing University, Chongqing 400044, China

Corresponding author: Jianjun Hu (hujianjun@cqu.edu.cn)

ABSTRACT In order to investigate the electromechanical coupling characteristics of the integrated electric drive system (IEDS) that consists of a surface-mounted permanent magnet synchronous motor (SPMSM) and a helical gear reducer, a transient dynamic model including the motor model and the driveline dynamic model is established. Based on this model, the interaction between the mechanical system and the electrical system of IEDS for electric vehicle is simulated and analyzed. To suppress the dynamic load of IEDS mechanical components caused by the sudden step electromagnetic torque during rapid acceleration, an active damping control strategy (ADCS) is proposed. With the effect of ADCS, the maximum mesh force and displacement of IEDS gear pair have reduced by 23.26% and 26.96% respectively, the maximum dynamic load of motor shaft and IEDS output shaft have reduced by 28.75% and 29.05% respectively. The simulation results indicate that ADCS could effectively suppress the driveline torsional vibration during rapid acceleration.

INDEX TERMS Integrated electric drive system, electromechanical coupling, torsional vibration, active damping control strategy.

I. INTRODUCTION

Electric vehicles (EVs) are becoming more and more popular due to the influence of global energy crisis. Compared with traditional internal combustion engine (ICE), electric motor can greatly reduce the dependence of the vehicle on the multi-speed transmission, which means the multi-speed transmission can be replaced by fix-speed reducer in EVs. The simple structure of reducer is beneficial to the integration of motor and reducer for further reducing the weight, volume and cost of EV powertrain system. Therefore, it is very significant to investigate the integrated motor and reducer system with high speed, high efficiency, high power density and lightweight. As shown in Figure1, the integrated electric drive system (IEDS) studied in this paper mainly includes a surface-mounted permanent magnet synchronous motor (SPMSM) with its controller, a helical gear reducer and an output shaft. Exploring the coupling characteristics

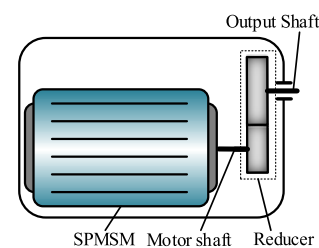The associate editor coordinating the review of this manuscript and approving it for publication was Zhuang Xu.

FIGURE 1. The configuration of the integrated electric drive system (IEDS).

between the electrical system and mechanical system of IEDS can provide theoretical basis for the optimization of mechanical structure and motor control strategy, which can further extend the life of IEDS and improve the vehicle driving comfort.

As an important component of IEDS, SPMSM is a nonlinear, strong coupling and multi-variable complex object. Almost modern SPMSM control systems are based on the rotor field-oriented vector control (RFVC) or direct torque

control (DTC) principle including the current loop and speed loop. In order to further improve the system performance, some novel speed control systems replace the traditional controllers of RFVC and DTC with more advanced controllers, such as adaptive controller [1], sliding mode variable structure controller [2], active disturbance rejection controller [3] and intelligent controller [4]–[6]. There are also some speed control systems that abandon the double closed-loop control structure of FRVC and DTC, such as model predictive controller [7]. Research on speed control system of PMSM has made considerable progress in recent years. However, the RFVC based on PI algorithm is still one of the most commonly used methods for SPMSM due to technical and cost reasons. Different from the traditional vehicle driveline with multi-speed transmission, the driveline of EV is relatively simple. As not equipped with clutch and hydraulic torque converter, the EV driveline presents underdamped characteristics. In addition, the torque response of electric motor is 10-50 times faster than that of internal combustion engine (ICE). During rapid launch process of EV, the sudden torque step produced by motor will lead to the driveline torsional vibration, where the low frequency longitudinal vibration occurs in the range of 2-10Hz [8]–[10]. In order to suppress the launch vibration of EV, reference [11]–[14] adopted feedforward control and feedback control to increase the system damping. In reference [15], a relatively small amount of rotation velocity offset was added to the traction motor to significantly reduce the resonant vibration with negligible impact to vehicle speed. Reference [16] proposed a wave superposition control strategy. The simulation results showed that the strategy was more effective than feedforward control in suppressing the launch vibration of hybrid electric vehicle. In reference [17], a torque control strategy based on fuzzy logic was proposed to suppress the driveline vibration of four-wheel drive electric vehicle. In addition, some other strategies could also effectively suppress the driveline torsional vibration of EV, such as linear quadratic regulator control [18], PI/PID control [19], pole placement control [20] and dynamic matrix control [21]. The above researches took advantage of the fast torque response of motor to suppress the driveline torsional vibration and achieved good results. However, the driveline model and motor model had been greatly simplified and unable to reflect the detailed dynamic response characteristics of drive system.

As another major component of IEDS, the gear transmission system is widely used in vehicle driveline with high efficiency and reliability. After long-term research by scholars all over the world, the complete theory system and modeling methods of gear transmission have been well established. Reference [22] established a coupled bending-torsion-shaft vibration model of helical gears, which took into account both time-varying mesh stiffness and mesh impact. In order to study the dynamic characteristics of high-speed helical gear transmission system in wind power gearbox, reference [23] established a bending-torsion coupling dynamic model and analyzed the effects of rotational speed, gear eccentricity and

bearing clearance on the vibration response characteristics of the transmission system. Reference [24] investigated the effects of sliding friction and profile modification on the mesh dynamic characteristics by finite element method. Reference [25], [26] studied the influence of average load, load fluctuation, mesh damping and backlash on the resonance characteristics of the transmission system, and then analyzed the relationship between average load and continuous mesh, unilateral impact and bilateral impact. In reference [27], the torsional vibration model of a single-degree-of-freedom gear pair was established to study the effects of time-varying mesh stiffness and engine speed fluctuation on the system stability. In current researches, the gear transmission system and SPMSM are always studied separately without considering the interaction between mechanical system and electrical system, which limits the further improvement of the dynamic performance of IEDS.

To deal with the above-mentioned issues, this paper establishes an electromechanical coupling model of IEDS including motor model and driveline dynamic model. Then, based on this model, the electromechanical dynamic response characteristics of IEDS under the conditions of rapid acceleration and impact load are simulated and analyzed. In order to suppress the driveline torsional vibration and ensure the vehicle's acceleration performance at the same time, an active damping control strategy (ADCS) based on motor torque compensation is proposed. The simulation results have confirmed the validity of the proposed strategy. This paper considers the following contributions and novelties:

1. A detailed transient dynamic model of IEDS is established to study the electromechanical coupling characteristics of the IEDS under the conditions of rapid acceleration and impact load, and the interaction between electric system and mechanical system is simulated and analyzed.

2. An active damping control strategy (ADCS) is proposed to suppress the torsional vibration of driveline during vehicle launch, and the effectiveness of the strategy is proved by simulation experiments.

A complete electromechanical coupling dynamic model of IEDS is established in Section II. In Section III, the electromechanical dynamic characteristics of IEDS during rapid acceleration and impact load condition are simulated and analyzed. In Section IV, according to the electromechanical coupling characteristics of IEDS obtained in Section III, an active damping control strategy is proposed to suppress the torsional vibration of the driveline and simulation experiment is conducted to verify the validity of the control strategy. Section V presents the final conclusions.

II. ELECTROMECHANICAL COUPLING DYNAMIC MODEL

The EV driveline equipped with IEDS is shown in Figure2, which consists of IEDS, final drive, differential, half-axle and wheel, etc. In order to study the electromechanical coupling characteristics of IEDS, detailed dynamic models of electrical system and mechanical system are established respectively.
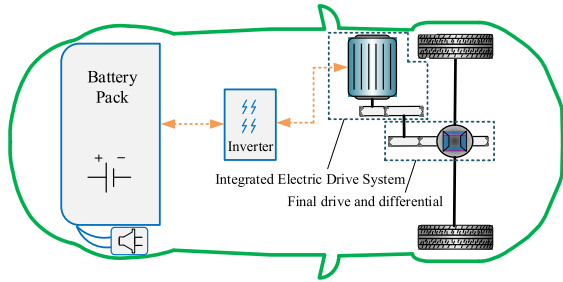
FIGURE 2. Electric vehicle driveline equipped with IEDS.

A. DYNAMIC MODEL OF SPMSM

The voltage equation of SPMSM expressed in the rotating dq frame can be given by

$$\begin{cases} U_d = Ri_d + L_s \dfrac{di_d}{dt} - \omega_e L_s i_q \\ U_q = Ri_q + L_s \dfrac{di_q}{dt} + \omega_e (L_s i_d + \psi_f) \end{cases} \tag{1}$$

where U_d and U_q are d-axis voltage and q-axis voltage respectively, i_d and i_q are d-axis current and q-axis current respectively, R is the stator resistance, L_s is the stator inductance and ω_e is the electrical angular speed.

The torque of the SPMSM can be calculated by

$$T_m = \frac{3}{2} P \psi_f i_q \tag{2}$$

where ψ_f is the permanent magnet flux linkage and P is the pole pair number.

B. SPEED CONTROL SYSTEM OF SPMSM

The maximum torque per ampere control (MTPAC) can make the SPMSM work more efficiently in the constant torque region at low speed, and the flux weakening control (FWC) can keep the SPMSM working stably in the constant power region at high speed. Therefore, the dq-axis reference currents are calculated by combining MTPAC and FWC in this paper.

1) STATOR DQ-AXIS REFERENCE CURRENTS

The stator voltage and current are both limited by system capability. The current limit circle and the voltage limit ellipse can be described as

$$i_d^2 + i_q^2 \le \left| \overrightarrow{i_s} \right|_{\max}^2 \tag{3}$$

$$\left(i_d + \frac{\psi_f}{L_s} \right)^2 + i_q^2 \le \left(\frac{\left| \overrightarrow{U_s} \right|_{\max}}{\omega_e L_s} \right)^2 \tag{4}$$

where $\left| \overrightarrow{i_s} \right|_{\max}$ is the maximum current limit and $\left| \overrightarrow{U_s} \right|_{\max}$ is the maximum effective voltage provided by the inverter.

a: MAXIMUM TORQUE PER AMPERE CONTROL

In the constant torque region, the unit stator current is expected to output as much electromagnetic torque as possible to improve the system efficiency. On the premise of

TABLE 1. The main electrical parameters of SPMSM.

Electrical parameters	Value	Unit
Maximum power	60	kW
Maximum Torque	200	Nm
Maximum speed	7000	rpm
Base Speed	2292	rpm
Stator resistance	0.153	Ω
Stator inductance	1.8	mH
Polar logarithm	4	—
Maximum current limit	150	A
Battery DC voltage	650	V

Equation (5) where C is a constant, the dq-axis reference currents are obtained by solving Equation (2) and Equation (5), as shown in Equation (6).

$$i_s = \sqrt{i_d^2 + i_q^2} = C \tag{5}$$

$$\begin{cases} i_{dref} = 0 \\ i_{qref} = i_s \end{cases} \tag{6}$$

b: FLUX WEAKENING CONTROL

As shown in Equation (7), ω_{et} is the maximum electrical angular speed that a motor can achieve in the constant torque region. And the base speed ω_{rt} can be described by Equation (8).

$$\omega_{et} = \frac{\left| \overrightarrow{U_s} \right|_{\max}}{\sqrt{\psi_f^2 + (L_s i_s)^2}} \tag{7}$$

$$\omega_{rt} = \frac{1}{P} \omega_{et} \tag{8}$$

The relationship between the q-axis reference current and the rotor angular velocity ω_r in the high-speed constant power region is described as Equation (9). Controlling $i_d = 0$ when the motor works at high speed, the motor can't work stably in the constant power region under the restriction of the stator voltage. Thus, it is necessary to control the d-axis current to weaken the magnetic field for improving the motor output torque, and then the d-axis reference current can be described as Equation (10).

$$i_{qref} = \frac{\omega_{rt}}{\omega_r} i_{s\,\max} \tag{9}$$

$$i_{dref} = -\sqrt{(i_{s\,\max})^2 - i_{qref}^2} = -\sqrt{1 - \left(\frac{\omega_{rt}}{\omega_r} \right)^2} i_{s\,\max} \tag{10}$$

The main parameters of the SPMSM are shown in Table 1. The numerical model of dq-axis reference currents is obtained by MTPAC and FWC, as shown in Figure 3.

2) DOUBLE CLOSED-LOOP PI CONTROL SYSTEM

Equation (1) reflects the dynamic coupling relationship between dq-axis currents and voltages. With the increase
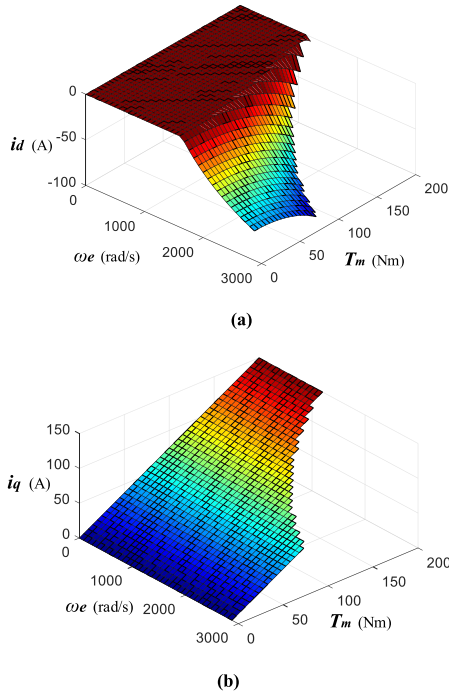
FIGURE 3. Numerical models of dq-axis reference currents. (a) Look-up table of d-axis reference current, (b) Look-up table of q-axis reference current.
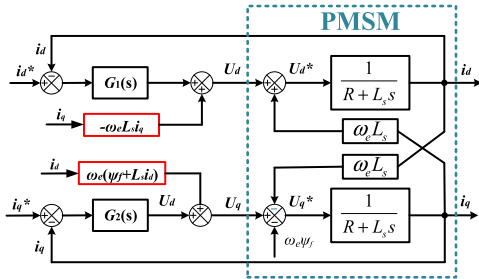

FIGURE 4. Current decoupling control.

of rotor speed, the proportion of coupling terms in stator voltages will also increase. To eliminate the influence of coupling terms on current control, the current decoupling control is adopted in this paper, as shown in Figure 4. In addition, the space vector pulse width modulation (SVPWM) is adopted to supply the dq-axis voltages by inverter.

With current decoupling control, the transfer function between the d-axis reference voltage and current can be described as

$$G_{md}(s) = \frac{i_d(s)}{U_d * (s)} = \frac{1}{R + L_s s} = \frac{1/R}{1 + L_s/Rs} \quad (11)$$

As shown in Figure 5, a PI controller is used as d-axis current controller, and the transfer function of $G_1(s)$ can be described as

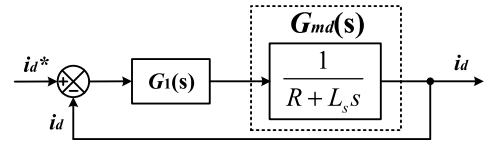$$G_1(s) = K_p + K_i \frac{1}{s} = \frac{K_p(\tau_1 s + 1)}{\tau_1 s} \quad (12)$$

FIGURE 5. PI controller of d-axis current.

where K_p is the proportionality coefficient, K_i is the integral coefficient, and $\tau_1 = K_p/K_i$.

The open-loop transfer function $G_{id}^c(s)$ between d-axis reference current and actual current can be described as

$$G_{id}^c(s) = G_1(s)G_{md}(s) = \frac{K_p(\tau_1 s + 1)}{\tau_1 s} \cdot \frac{1/R}{1 + L_s/Rs} \quad (13)$$

In order to make the actual current follow the reference current better, this paper adjusts the open-loop transfer function $G_{id}^c(s)$ to an integral function. Thus the parameters of the current PI controller must satisfy Equation (14).

$$\tau_1 = L_s/R \quad (14)$$

Then, Equation (13) can be described as

$$G_{id}^c(s) = \frac{K_p}{R\tau_1 s} = \frac{K_p/L_s}{s} \quad (15)$$

The relationship between the zero amplitude crossing frequency ω_c of the open-loop transfer function $G_{id}^c(s)$ and the proportional coefficient K_p can be described as

$$K_p = L_s\omega_c \quad (16)$$

The parameters of d-axis current PI controller can be obtained by choosing appropriate zero amplitude crossing frequency. Similarly, the parameters of q-axis current PI controller can be obtained. In this paper, the speed controller is also a PI controller. However, the rotor speed response is not only relevant with the electromagnetic torque, but also the transmission system and external load, which makes the relationship between motor torque and rotor speed can't be expressed in the form of transfer function. Therefore, the parameters of the speed PI controller are selected through multiple simulation experiments. The parameters of the three PI controllers are shown in Table 2.

TABLE 2. Parameters of current loop PI controllers and speed loop PI controller.

	K_p	K_i
d-axis current loop PI controller	14.67	1222.5
q-axis current loop PI controller	14.67	1222.5
Speed loop PI controller	0.2	1.1×10^{-3}

C. DYNAMIC MODEL OF THE EV DRIVELINE
The motion model of IEDS gear pair is illustrated in Figure 6. The internal excitation in gear mesh process mainly includes time-varying mesh stiffness and mesh error. Many researchers utilized the gear rotation period to describe the
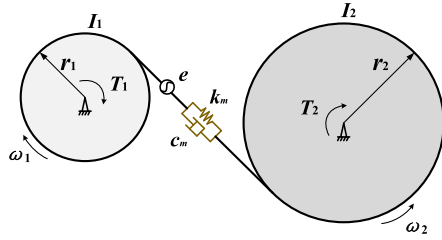
FIGURE 6. Torsional vibration analysis model of IEDS gear pair.

mesh stiffness in time domain before, but the rotation speed of vehicle driveline varies with time, which makes the mesh stiffness inconvenient to express with respect to time. In this study, the time-varying mesh stiffness and mesh error are described in terms of the gear rotation angles by calculating the length of contact line during mesh.

According to the mesh characteristics of helical gear pair, the mesh stiffness k_{mi} of i_{th} ($i = 1, 2, \cdots \text{ceil}(\varepsilon_\gamma)$) mesh tooth pair can be described as Equation (17) and (18) [28], [29].

When $\varepsilon_\alpha \geq \varepsilon_\beta$,

$$
k_{mi} = \begin{cases}
\int_{a_1}^{b_1} k_u dL, & 0 \leq s < \varepsilon_\beta p_b \\
\int_{a_2}^{b_2} k_u dL, & \varepsilon_\beta p_b \leq s < \varepsilon_\alpha p_b \\
\int_{a_3}^{b_3} k_u dL, & \varepsilon_\alpha p_b \leq s < \varepsilon_\gamma p_b \\
0, & \varepsilon_\gamma p_b \leq s < \text{ceil}(\varepsilon_\gamma) p_b
\end{cases}
\tag{17}
$$

where $s = r_{b1} \mod (\theta_1 + 2(i-1)\pi/Z_1, 2\text{ceil}(\varepsilon_\gamma)\pi/Z_1)$, $a_1 = (\varepsilon_\beta p_b - s)/\sin\beta_b$, $b_1 = b/\cos\beta_b$, $a_2 = 0$, $b_2 = b/\cos\beta_b$, $a_3 = 0$, $b_3 = (\varepsilon_\gamma p_b - s)/\sin\beta_b$.

When $\varepsilon_\alpha < \varepsilon_\beta$,

$$
k_{mi} = \begin{cases}
\int_{a_1}^{b_1} k_u dL, & 0 \leq s < \varepsilon_\alpha p_b \\
\int_{a_2}^{b_2} k_u dL, & \varepsilon_\alpha p_b \leq s < \varepsilon_\beta p_b \\
\int_{a_3}^{b_3} k_u dL, & \varepsilon_\beta p_b \leq s < \varepsilon_\gamma p_b \\
0, & \varepsilon_\gamma p_b \leq s < \text{ceil}(\varepsilon_\gamma) p_b
\end{cases}
\tag{18}
$$

where $s = r_{b1} \mod (\theta_1 + 2(i-1)\pi/Z_1, 2\text{ceil}(\varepsilon_\gamma)\pi/Z_1)$, $a_1 = (\varepsilon_\beta p_b - s)/\sin\beta_b$, $b_1 = b/\cos\beta_b$, $a_2 = (\varepsilon_\beta p_b - s)/\sin\beta_b$, $b_2 = (\varepsilon_\gamma p_b - s)/\sin\beta_b$, $a_3 = 0$, $b_3 = (\varepsilon_\gamma p_b - s)/\sin\beta_b$.

In Equation (17) and (18), 'ceil' function rounds ε_γ to the nearest (higher) integer value and mod (x, y) is residual function. ε_α and ε_β are transverse and overlap contact ratios, respectively. ε_γ is the contact ratio and $\varepsilon_\gamma = \varepsilon_\beta + \varepsilon_\alpha$. Z_1, r_1 and θ_1 are teeth number, basic circle radius and angular displacement of the driving gear, respectively. p_b is the base pitch, b is the face width, β_b is the base helix angle and k_u is the mesh stiffness per unit length along the contact line. Then,

the total mesh stiffness can be calculated as

$$
k_m = \sum_{i=1}^{\text{ceil}(\varepsilon_\gamma)} k_{mi}
\tag{19}
$$

The parameters of the gear pair are shown in Table 3. The time-varying mesh stiffness can be calculated by Equation (19) and (20) as given in Figure 7.

TABLE 3. Fundamental parameters of the gear pair.

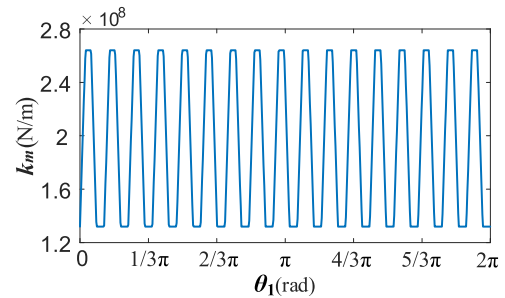| Mechanical parameters	Symbol	Driving gear	Driven gear	Unit
Tooth number	Z	17	28	—
Normal module	m_n	3	3	mm
End module	m_t	3.19	3.19	mm
Face width	b	20	20	mm
Normal pressure angle	α_n	20	20	deg
End pressure angle	α_t	21.17	21.17	deg
Helix angle	β	20	20	deg

FIGURE 7. Time-varying mesh stiffness of IEDS gear pair.

The empirical formula for mesh damping is [30]

$$
c_m = 2\xi_m \sqrt{k_{ma} m_1 m_2/(m_1 + m_2)}
\tag{20}
$$

where k_{ma} is the average mesh stiffness, ξ_m is the mesh damping ratio, and m_i is the mass of gear i.

The error excitation is

$$
e = e_m + e_r \sin(Z_1 \theta_1 + \delta)
\tag{21}
$$

where e_m and e_r are the constant value and amplitude value of mesh error, which are related to the manufacturing accuracy of the gears, and δ is the initial phase of mesh error.

Ignoring the influence of backlash on gear transmission, the mesh force can be described as

$$
F_m = c_m(R_1\dot{\theta}_1 - R_2\dot{\theta}_2 - \dot{e}) + k_m(R_1\theta_1 - R_2\theta_2 - e)
\tag{22}
$$

As shown in Figure 8, a 6-DOF torsional vibration model of the EV driveline is established based on the lumped parameter method.
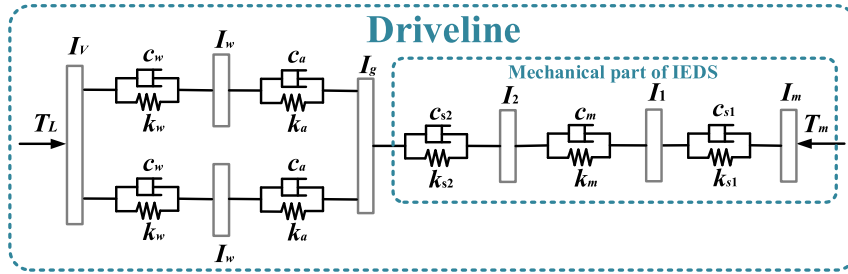
FIGURE 8. 6-DOF torsional vibration model of the driveline.

TABLE 4. The main mechanical parameters of the driveline.

Symbol	Quantity	Value	Unit
I_m	Moment of inertia of rotor and motor shaft	0.035	Kg·m^2
I_1	Moment of inertia of IEDS driving gear	1.67×10^{-4}	kg·m^2
I_2	Moment of inertia of IEDS driven gear	1.2×10^{-3}	kg·m^2
I_g	Equivalent moment of inertia of final drivel and differential	8×10^{-3}	kg·m^2
I_w	Moment of inertia of wheel	0.915	kg·m^2
I_V	Equivalent moment of inertia of vehicle	139.8	kg·m^2
k_{s1}	Torsional stiffness of motor shaft	8×10^4	Nm/rad
k_u	Mesh stiffness per unit length along the contact line	1×10^{10}	Nm/rad
k_{s2}	Torsional stiffness of IEDS output shaft	2×10^5	Nm/rad
k_a	Torsional stiffness of half-axle	8×10^3	Nm/rad
k_w	Torsional stiffness of wheel	4.5×10^3	Nm/rad
c_{s1}	Torsional damping ratio of motor shaft	2	Nm·s/rad
c_m	Gear pair mesh damping	800	N /(m/s)
c_{s2}	Torsional damping ratio of IEDS output shaft	2	Nm·s/rad
c_a	Torsional damping ratio of half-axle	8	Nm·s/rad
c_w	Torsional damping ratio of wheel	20	Nm·s/rad
i_0	Final drive ratio	4.06	—
m	Vehicle mass	1400	kg
r	Wheel radius	0.316	m
f	Rolling resistance	0.015	—
Cd	Aerodynamic drag factor	0.3	—
A	Front section	1.746	m^2
α	slope angle	0	deg

The mathematical expression of the 6-DOF torsional vibration model is

$$
\begin{cases}
I_m\ddot{\theta}_m + c_{s1}(\dot{\theta}_m - \dot{\theta}_1) + k_{s1}(\theta_m - \theta_1) = T_m \\
I_1\ddot{\theta}_1 - c_{s1}(\dot{\theta}_m - \dot{\theta}_1) - k_{s1}(\theta_m - \theta_1) + R_1 F_m = 0 \\
I_2\ddot{\theta}_2 + c_{s2}(\dot{\theta}_2 - \dot{\theta}_g) + k_{s2}(\theta_2 - \theta_g) - R_2 F_m = 0 \\
I_g\ddot{\theta}_g - c_{s2}(\dot{\theta}_2 - \dot{\theta}_g) - k_{s2}(\theta_2 - \theta_g) + 2/i_0 \cdot c_a(\dot{\theta}_g/i_0 - \dot{\theta}_w) \\
\qquad +2/i_0 \cdot k_a(\theta_g/i_0 - \theta_w) = 0 \\
I_w\ddot{\theta}_w - c_a(\dot{\theta}_g/i_0 - \dot{\theta}_w) - k_a(\theta_g/i_0 - \theta_w) + c_w(\dot{\theta}_w - \dot{\theta}_V) \\
\qquad +k_w(\theta_w - \theta_V) = 0 \\
I_V\ddot{\theta}_V - 2c_w(\dot{\theta}_w - \dot{\theta}_V) - 2k_w(\theta_w - \theta_V) = -T_L
\end{cases}
$$
(23)

where T_m is the electromagnetic torque generated by SPMSM, T_L is the external load that applied to the equivalent moment of inertia of vehicle. T_L can be described as

$$
T_L = (mgf\cos\alpha + \frac{C_D A}{21.15}V^2 + mg\sin\alpha)/r \quad (24)
$$

The parameters in Equation (23) and (24) are given in Table 4.

The motion equation of the torsional system can be written in matrix form as

$$
\mathbf{M}\ddot{\boldsymbol{\theta}} + \mathbf{C}\dot{\boldsymbol{\theta}} + \mathbf{K}\boldsymbol{\theta} = \mathbf{T} \quad (25)
$$

where $\mathbf{M}$ is the inertia matrix, $\mathbf{C}$ is the damping matrix, $\mathbf{K}$ is the stiffness matrix, $\boldsymbol{\theta}$ is the rotational displacement vector
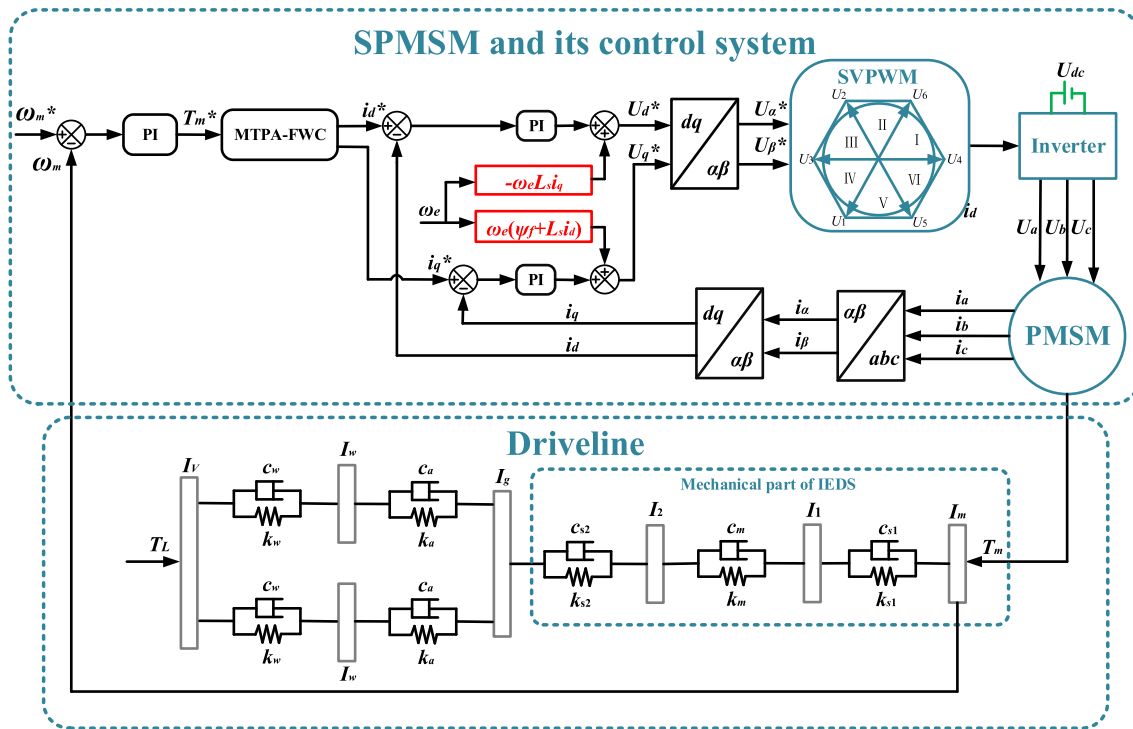
FIGURE 9. Electromechanical coupling dynamic model of the EV equipped with IEDS.

TABLE 5. Natural frequencies of driveline.

Mode order	0	1	2	3	4	5
Frequency /Hz	0	7.6	22.8	514.1	2527.1	6095.7

and **T** is the torque excitation vector. Appendix I gives the details of **M**, **C**, **K**, θ and **T** matrixes.

According to Equation (25), the free vibration equation of the system can be described as Equation (26) and Equation (27) without considering the damping and external excitation.

$$\mathbf{M}\ddot{\theta} + \mathbf{K}\theta = 0 \qquad (26)$$

$$(\mathbf{K} - \omega^2\mathbf{M})\theta = 0 \qquad (27)$$

Replacing the time-varying mesh stiffness with mean stiffness, the natural frequencies of the system are obtained by calculating the eigenvalues of Equation (27), as shown in Table 5. As a positive semi-definite system, the zeroth-order frequency is 0 Hz and the mechanical components will rotate without vibration in this mode. And when the gear mesh frequency approaches the other natural frequencies, the driveline will resonate. The speeds of the driving gear corresponding to the 1-5th order natural frequencies are 27rpm, 81rpm, 1814rpm, 8919rpm and 21514rpm, respectively. It can be seen that the speeds corresponding to the 5-6th order natural frequencies have exceeded the maximum speed of the SPMSM.

III. SIMULATION AND ANALYSIS OF ELECTROMECHANICAL COUPLING EFFECT OF IEDS

As common variables, the speed and torque of motor shaft are transmitted between the SPMSM and driveline in real time, as shown in Figure 9. The dynamic simulation of the model is conducted with MATLAB/Simulink and solved by the fourth-order Runge-Kutta method.

A. ELECTROMECHANICAL COUPLING DYNAMIC CHARACTERISTICS OF IEDS DURING RAPID ACCELERATION

The initial speed and target speed of motor shaft is set at 0rpm and 4000rpm respectively, and the external load during acceleration is shown in Figure 10. The electromagnetic torque generated by SPMSM is shown in Figure 11, which
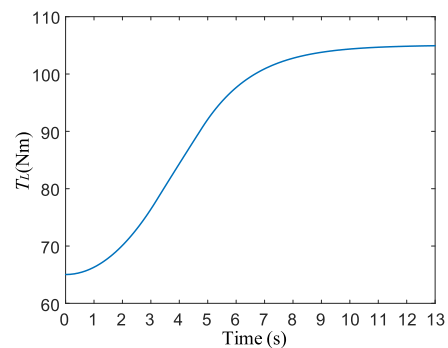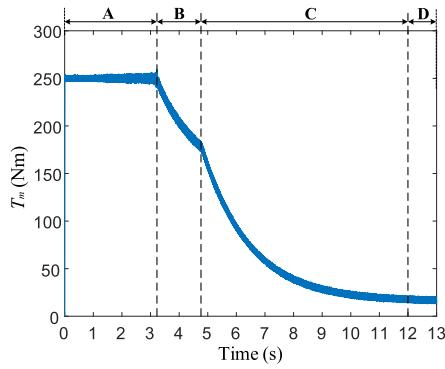

FIGURE 10. External load.

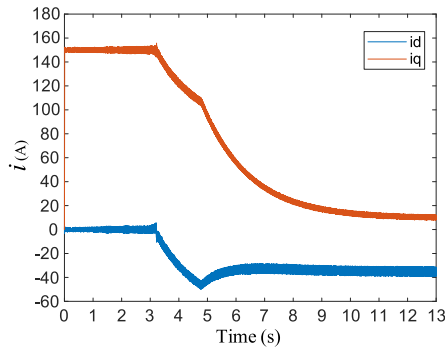**FIGURE 11. Electromagnetic torque.**

FIGURE 12. dq-axis currents.

can be roughly divided into 4 areas. When rapid acceleration begins, the electromagnetic torque quickly reaches the maximum value of 250Nm to drive the vehicle, as shown in area A. At about 3.2s, the rotor speed reaches the motor base speed of 2292rpm. Under the control of FWC, the SPMSM transits from constant torque region to constant power region, as shown in area B. With speed closed-loop PI control, the electromagnetic torque decrease gradually when the rotor speed approaches the target speed, as shown in area C. In area D, the motor achieves the target speed and the torque tends to be constant. Figure 12 shows the dq-axis currents

of the SPMSM during acceleration. Under the combined control of MTPAC and FWC, when rotor speed is below base speed, $id = 0$, and when rotor speed exceeds base speed, $id < 0$. Figure 13 shows the speed of rotor, IEDS gear pair and vehicle. Because of the weak damping of driveline, step electromagnetic torque excites strong torsional vibration of driveline during vehicle launch. As a result, the speed of rotor and gear pair fluctuates sharply and the vehicle surges. At about 2.5s, the driveline resonates because the mesh frequency of the IEDS gear pair approaches the 3nd order frequency of driveline. Figure 14 (a) shows the disordered three-phase stator current when the rotor speed fluctuates greatly during vehicle launch and Figure 14 (b) shows the stationary three-phase stator current when the rotor speed is stable.

The dynamic mesh force and mesh displacement of IEDS gear pair during the acceleration are shown in Figure 15 and Figure16, respectively. At the beginning of acceleration, the sudden torque step produced by SPMSM causes the dynamic mesh force and mesh displacement oscillation phenomenon during vehicle launch. The maximum value of the dynamic mesh force reaches 1.72×10^4N, which is approximately 1.69 times the static theoretical value. Then the oscillation amplitude gradually decreases due to the effect of system damping. Under the excitation of time-varying mesh stiffness and mesh error, the dynamic mesh force fluctuates all the time. As the rotor speed approaches the target speed, the mesh force decreases with the decreasing electromagnetic torque. At about 2.5s, the driveline resonance causes violent oscillation of the mesh displacement and mesh force. As shown in Figure 17(a), frequency domain analysis of mesh force during 0-1s shows that the vibration energy mainly concentrates on zeroth-order frequency. Except for this, the main vibration frequencies are 7.5Hz and 22.4Hz, which are close to the 1st and 2nd order frequencies of driveline. The frequency domain analysis of the mesh force during 12-13s is shown in Figure 17(b). The main vibration frequencies are 1134 Hz and 2268 Hz, which are approximately one and two times the mesh frequency of IEDS gear pair respectively. The dynamic torque transmitted by motor shaft and output shaft
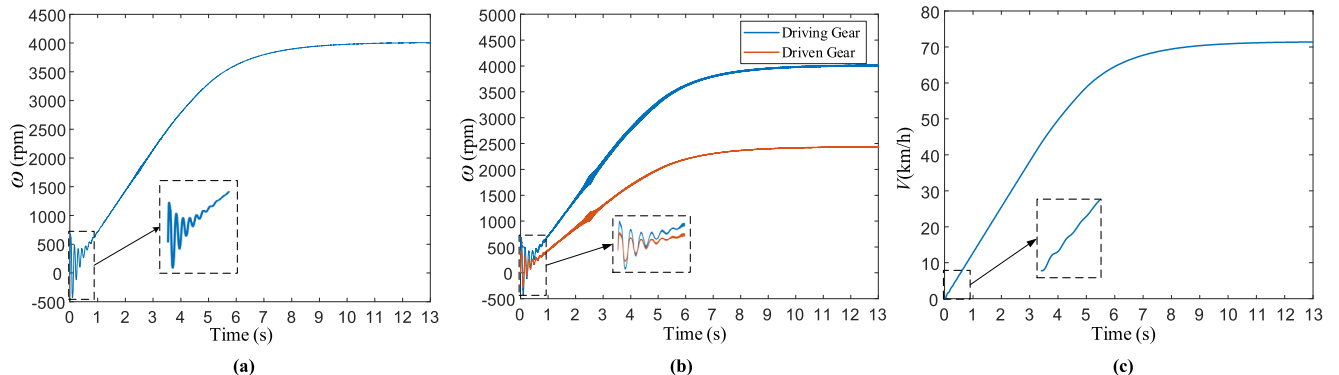

FIGURE 13. Speed of rotor, IEDS gear pair and vehicle. (a) Rotor speed, (b) Speed of IEDS gear pair, (c) Vehicle speed.
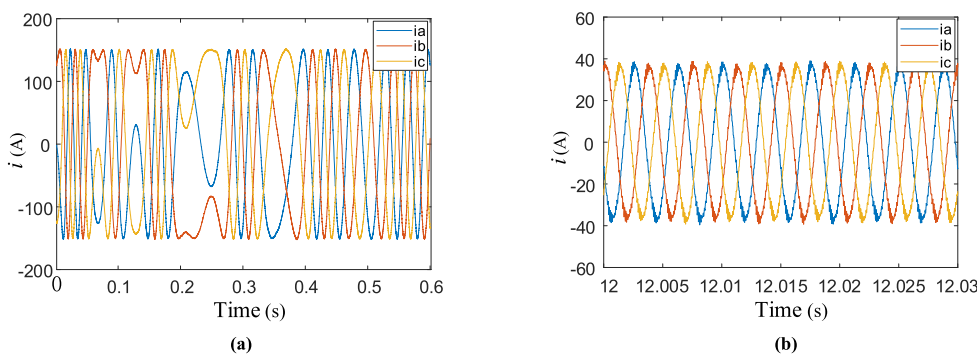
FIGURE 14. Three-phase stator current. (a) Disordered three-phase stator current during vehicle launch, (b) Stationary three-phase stator current.
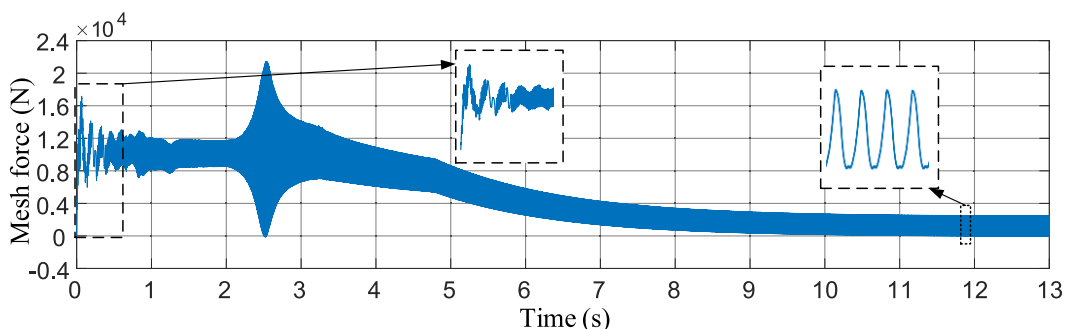

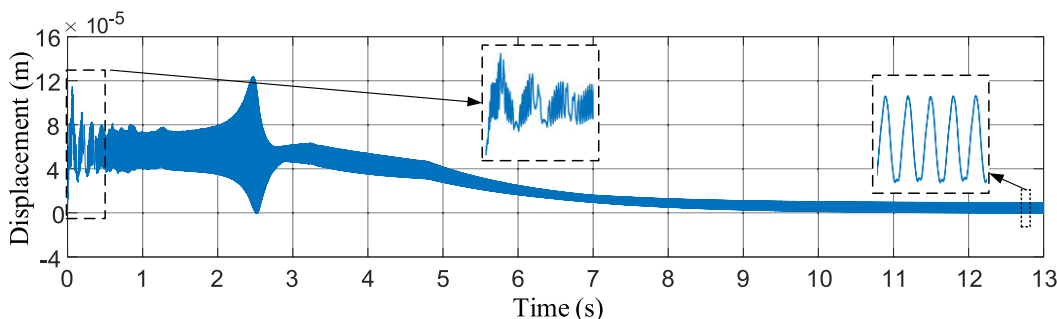**FIGURE 15.** Mesh force of IEDS gear pair.

FIGURE 16. Mesh displacement of IEDS gear pair.

of IEDS are shown in Figure 18, and the diversification trend of the dynamic torques is consistent with that of the gear pair mesh force.

B. EFFECT OF IMPACT LOAD ON THE DYNAMIC CHARACTERISTICS OF IEDS

The electromechanical dynamic responses of IEDS under impact load condition are simulated and analyzed in this paper. The initial rotor speed is 4000rpm and the constant external load that applied to equivalent moment of inertia of vehicle is 100Nm. A 500Nm impact load is applied to wheels and lasts for 0.1s, as shown in Figure 19. The working mode of SPMSM includes torque control mode and speed control mode. In torque control mode, the motor only adjusts the output torque to achieve the target torque. And in speed

control mode, the motor automatically adjusts the output torque to make the rotor achieve the target speed. Figure 20, Figure 21 and Figure 22 compare the electromagnetic torque, rotor speed and meshing force of IEDS gear pair in speed control mode and torque control mode, respectively. In torque control mode, the impact load excites torsional vibration of driveline when the motor maintains constant torque output. In speed control mode, the fluctuating electromagnetic torque produced by SPMSM effectively suppress the rotor speed fluctuation and reduce the dynamic mesh force of IEDS gear pair.

IV. ACTIVE DAMPING CONTROL STRATEGY

During rapid acceleration, the high response of motor torque will excite violent torsional vibration of driveline. The most
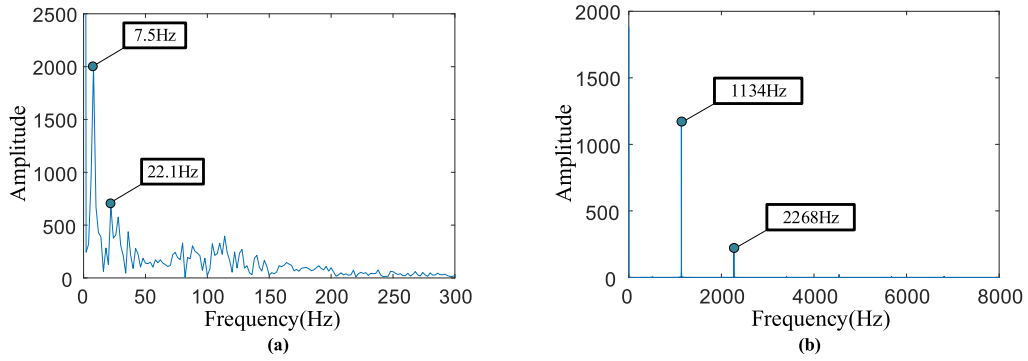
FIGURE 17. Frequency domain analysis of mesh force. (a) Frequency domain analysis of mesh force during 0-1s, (b) Frequency domain analysis of mesh force during 12-13s.
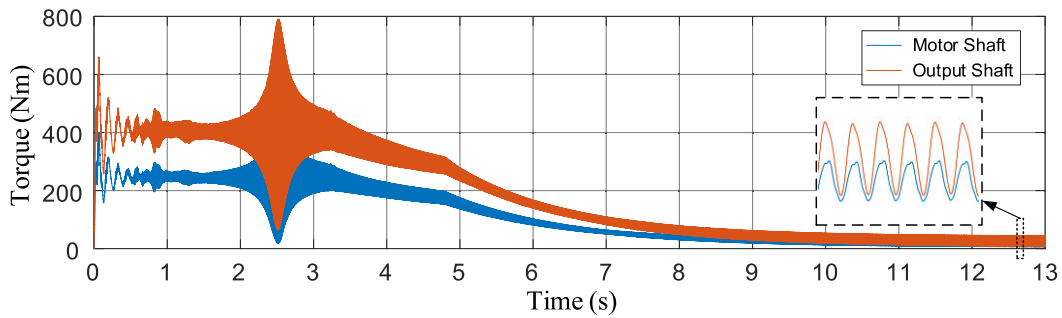

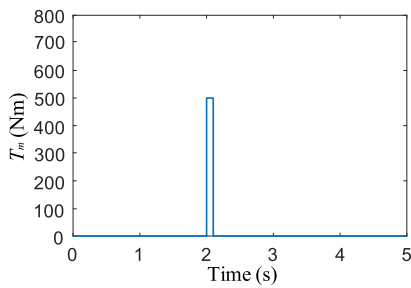**FIGURE 18.** Dynamic torque transmitted by motor shaft and output shaft of IEDS.

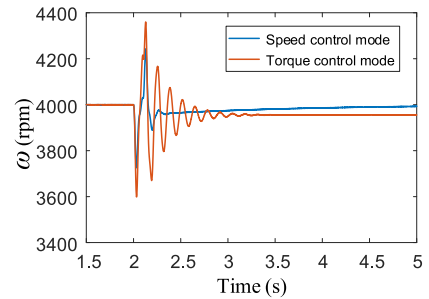**FIGURE 19.** Impact load applied to wheels.
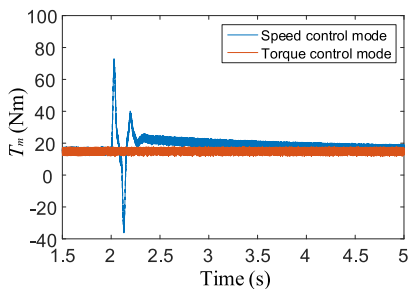

FIGURE 21. Rotor speed.

FIGURE 20. Electromagnetic torque of SPMSM.

direct way to suppress the torsional vibration is to reduce the motor torque, which will also reduce the dynamic performance of vehicle. In order to suppress the torsional vibration

and ensure the acceleration ability of IEDS at the same time, an active damping control strategy (ADCS) is proposed in this paper based on the high response of motor torque.

A. CONTROL STRATEGY DESIGN
As shown in Figure 17(a), the main vibration frequencies of mesh force during 0-1s are 7.5Hz and 22.4Hz, which are close to the 1st and 2nd order frequencies of driveline. Thus the aim of ADCS is to weaken the torsional vibration at these two frequencies. The essence of suppressing the torsional vibration during rapid acceleration is to stabilize the system's acceleration value quickly. As shown in Figure 23, the acceleration signal is extracted by motor shaft speed, and
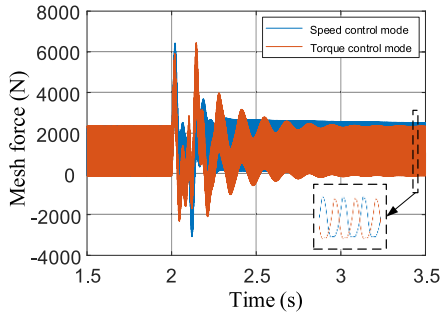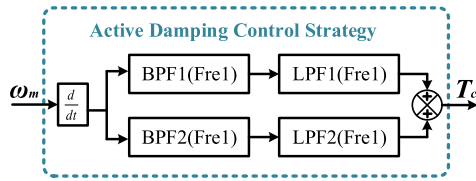
FIGURE 22. Mesh force of IEDS gear pair.

FIGURE 23. Active damping control strategy.

TABLE 6. Parameter setting of the filters.

ξ_1	ξ_2	ω_1	ω_2	K_{LPF1}	K_{LPF2}
1	1	7.6	22.8	6	2

FIGURE 24. Bode diagram the filters. (a) BPF1, (b) BPF2, (c) LPF1, (d) LPF2.

then processed by two parallel band-pass filters (BPFs) and low-pass filters (LPFs). Thus the compensation torque T_c is formed and will be added to the electromagnetic torque.

BPF can provide the oscillation level signal of each resonance frequency. Two second-order BPFs are selected and the transfer functions of them are shown in Equation (28). The central frequencies of the two BPFs are the 1st and 2nd order frequencies of the driveline, respectively.

$$\begin{cases} G_{BPF1}(s) = \dfrac{2\xi_1 \cdot (2\pi\omega_1)s}{s^2 + 2\xi_1 \cdot (2\pi\omega_1)s + (2\pi\omega_1)^2} \\ G_{BPF2}(s) = \dfrac{2\xi_2 \cdot (2\pi\omega_2)s}{s^2 + 2\xi_2 \cdot (2\pi\omega_2)s + (2\pi\omega_2)^2} \end{cases} \quad (28)$$

LPF not only filters the high-frequency portion of the motor shaft acceleration signal, but also introduces the phase lagging and filter gain at the same time. Proper selection of cutoff frequency and filter gain could result in increased damping of the driveline [31], [32]. Two first-order LPFs are selected and the transfer functions can be described as

$$\begin{cases} G_{LPF1}(s) = \dfrac{K_{LPF1}}{s + 2\pi\omega_1} \\ G_{LPF2}(s) = \dfrac{K_{LPF2}}{s + 2\pi\omega_2} \end{cases} \quad (29)$$

The parameters of the BPFs and LPFs are selected as Table 6. In addition, the Bode plots of the filters are shown in Figure 24, which shows the frequency response characteristics of each filter.

Based on the electromechanical coupling dynamic model in Figure 9, the new dynamic model with ADCS is established
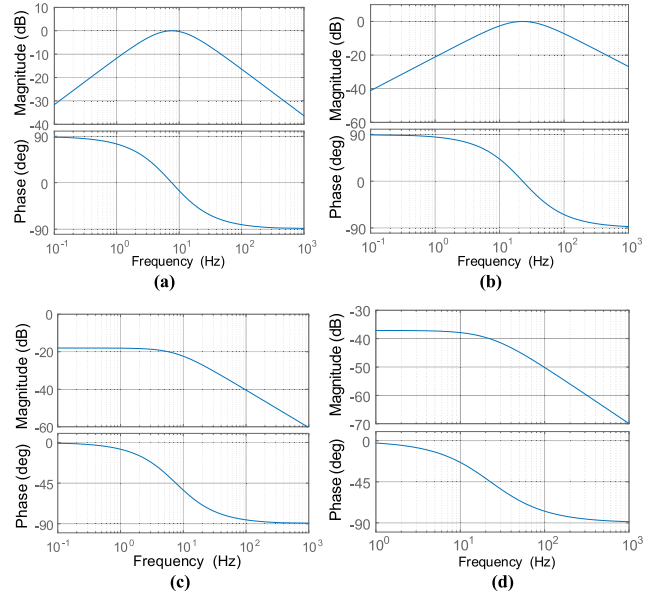
as shown in Figure 25. The motor shaft speed ω_m is used as the input signal of ADCS. Then the compensation torque T_c formed by ADCS is added to the electromagnetic torque of PMSM to suppress the acceleration fluctuation, which is equivalent to increase the system damping.

B. SYSTEM STABILITY AND CONVERGENCE VALIDATION

After adding ADCS to the control system, the stability and convergence of the control system needs to be verified. In this paper, the poles distribution of the simplified transfer function of the control system will be used to verify its stability. Without external load, Figure 26 illustrates the closed-loop control system with ADCS. $G(s)$ is the transfer function between the electromagnetic torque T_m and the motor shaft speed ω_m, $H(s)$ is the transfer function between the motor shaft acceleration α_m and the compensation torque T_c.

The transfer function $G(s)$ of driveline is derived by Equation (23). Ignoring the mesh error of IEDS gear pair and replacing the time-varying mesh stiffness with mean stiffness, Equation (23) can be transformed into a state equation. The angular displacements and speeds of the system components are defined as the state variables, as shown in Equation (30).

$$\mathbf{x}(t)=[x_1, x_2, x_3, x_4, x_5, x_6, x_7, x_9, x_{10}, x_{11}, x_{12}]^\mathrm{T}=\begin{bmatrix} \boldsymbol{\theta} \\ \dot{\boldsymbol{\theta}} \end{bmatrix}_{12\times1} \quad (30)$$

Thus, Equation (19) is transformed into the state equation that can be described as

$$\begin{cases} \dot{\mathbf{x}}(t) = \mathbf{A}\mathbf{x}(t) + \mathbf{B}\mathbf{u}(t) \\ \mathbf{y}(t) = \mathbf{x}(t) \end{cases} \quad (31)$$

where $\mathbf{A} = \begin{bmatrix} \mathbf{O}_{6\times6} & \mathbf{I}_{6\times6} \\ -\mathbf{M}^{-1}\mathbf{K} & -\mathbf{M}^{-1}\mathbf{C} \end{bmatrix}_{12\times12}$, $\mathbf{B} = \begin{bmatrix} \mathbf{O}_{6\times6} \\ \mathbf{M}^{-1} \end{bmatrix}_{12\times6}$, $\mathbf{u}(t)$ is the input vector and $\mathbf{y}(t)$ is the output vector.
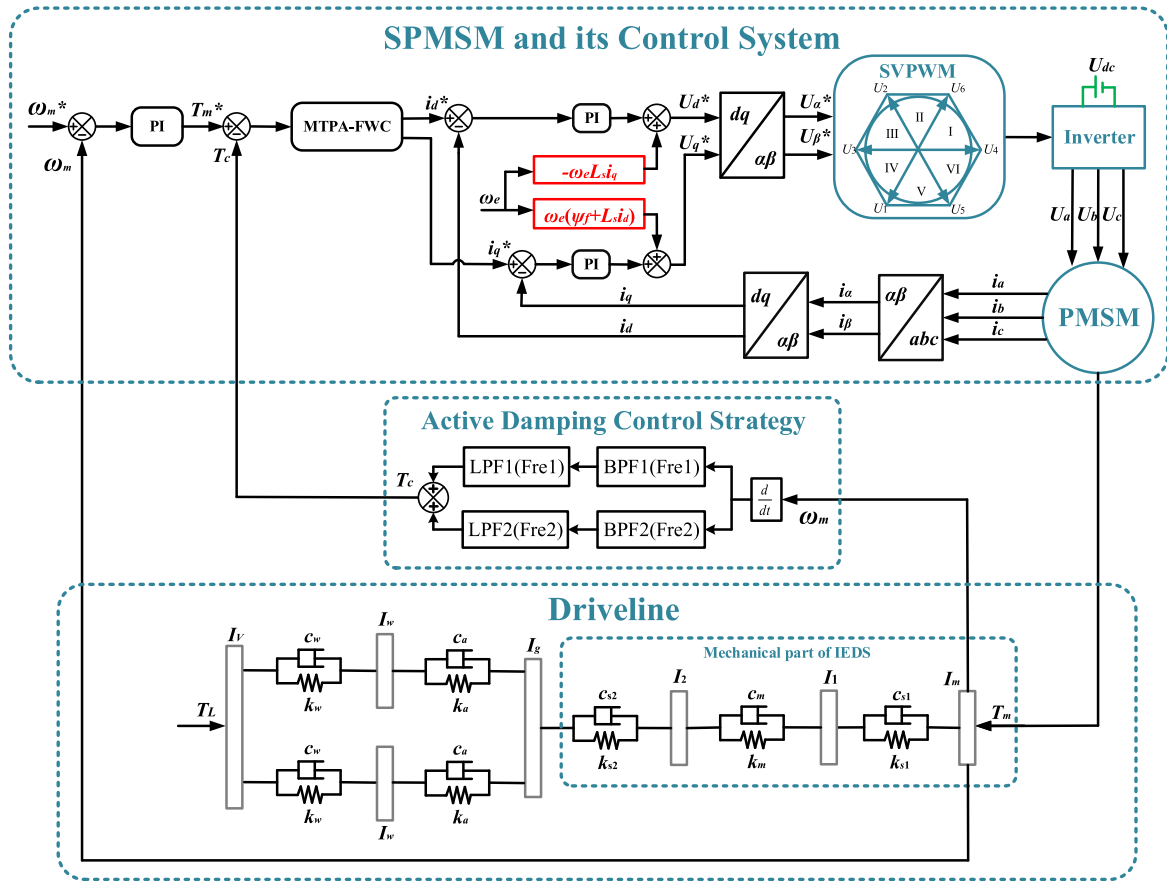
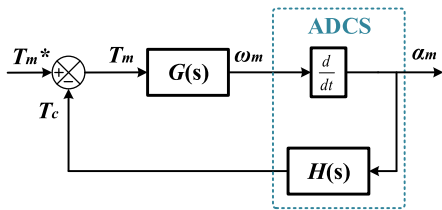**FIGURE 25.** Electromechanical coupling dynamic model with ADCS.

FIGURE 26. Transfer function model of driveline with ADCS.

The initial value $x_n(0)$ of each state variable is set as 0. By using Laplace transform, Equation (31) can be described as

$$s\mathbf{X}(s) = \mathbf{A}\mathbf{X}(s) + \mathbf{B}\mathbf{U}(s) \tag{32}$$

Thus

$$\mathbf{Y}(s) = \mathbf{X}(s) = (s\mathbf{I} - \mathbf{A})^{-1}\mathbf{B}\mathbf{U}(s) \tag{33}$$

Then, the transfer function matrix of the input vector and output vector is obtained as

$$\mathbf{W}(s) = [(s\mathbf{I} - \mathbf{A})^{-1}\mathbf{B}] \tag{34}$$

The transfer function $G(s)$ between the electromagnetic torque and the motor shaft speed is $\mathbf{W}(7,1)$. The open-loop transfer function between the electromagnetic torque and the motor shaft acceleration can be described as

$$K(s) = G(s)s \tag{35}$$

The transfer function between the motor shaft acceleration and the compensation torque can be described as

$$H(s) = G_{BPF1}(s)G_{LPF1}(s) + G_{BPF2}(s)G_{LPF2}(s) \tag{36}$$

The closed-loop transfer function between the reference electromagnetic torque T_m^* and the motor shaft acceleration α_m can be described as

$$F(s) = \frac{K(s)}{1 + K(s)H(s)} = \frac{G(s)s}{1 + G(s)H(s)s} \tag{37}$$

After resolving the transfer function matrix by MATLAB, $G(s)$, $K(s)$ and $F(s)$ are obtained as shown in Appendix II. The pole distribution of the open-loop transfer function $G(s)$ and the closed-loop transfer function $F(s)$ of the system is shown in Table 7. It can be seen that the transfer function increases by 3 pairs of poles with ADCS, but the increased poles are still distributed on the left side of the imaginary axis, which means system is still stable. When the input of the system is unchanged, the output will converge gradually and tend to be stable rather than divergent.

TABLE 7. Pole distribution of the transfer function model.

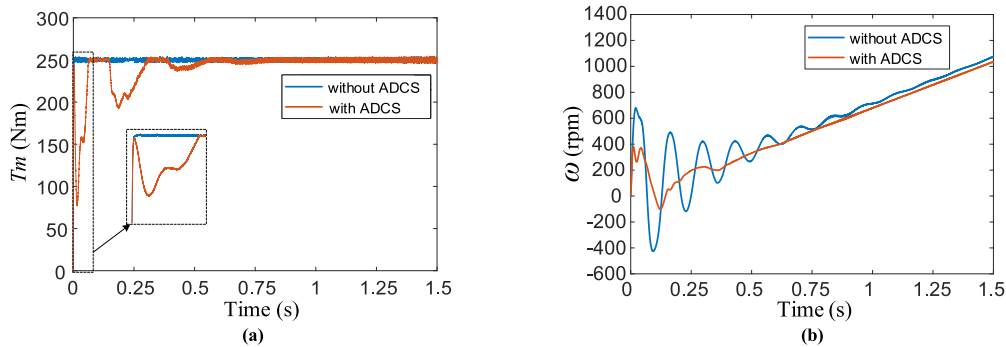|	1	2	3	4	5	6	7	8
$K(s)$	$-4\pm47i$	$-15\pm142i$	$-128\pm3228i$	$-1860\pm15844i$	$-7156\pm37428i$		—	—
$F(s)$	$-28, -81$	$-4\pm43i$	$-21\pm137i$	$-50\pm33i$	$-178\pm145i$	$-128\pm3229i$	$-1860\pm15844i$	$-7156\pm37428i$

FIGURE 27. Electromagnetic torque and rotor speed. (a) Electromagnetic torque, (b) Rotor speed.
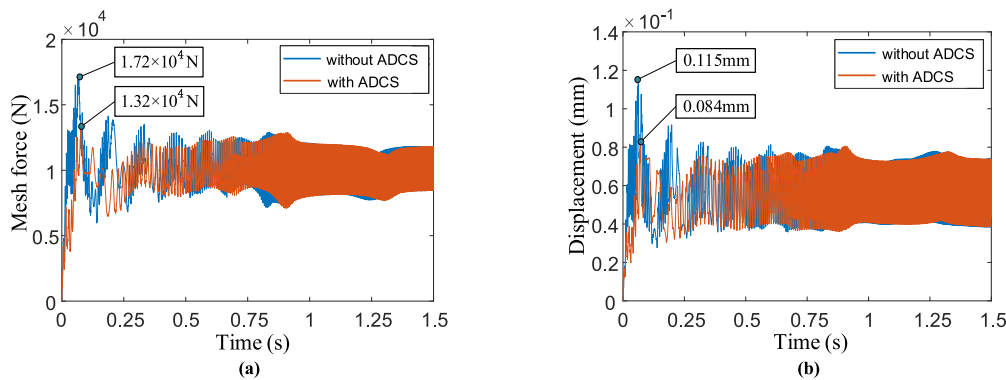
FIGURE 28. Mesh force and mesh displacement of IEDS gear pair. (a) Mesh force of IEDS gear pair, (b) Mesh displacement of IEDS gear pair.
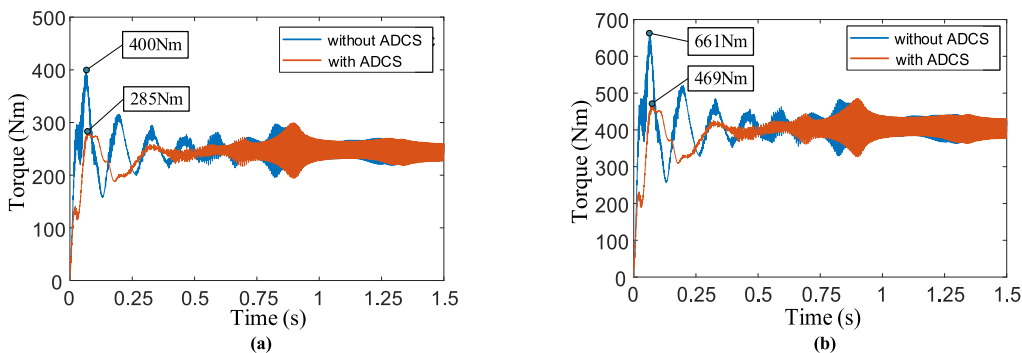
FIGURE 29. Dynamic torque transmitted by motor shaft and IEDS output shaft. (a) Dynamic torque transmitted by motor shaft, (b) Dynamic torque transmitted by IEDS output shaft.

C. SIMULATION RESULTS

Based on the active damping control strategy proposed in this paper, the simulation experiment is carried out. Figure 27(a) shows the electromagnetic torque of SPMSM. The motor

generate a ripple electromagnetic torque with the compensation torque computed by ADCS. Figure 27(b) shows the rotor speed of SPMSM. It can be seen that the rotor speed fluctuation decreases much more rapidly with ADCS than

TABLE 8. Dynamic load and deformation of the mechanical system of IEDS.

	Without ADCS	With ADCS	Improvement
Maximum mesh force of the gear pair (N)	1.72×10^4	1.32×10^4	23.26%
Maximum mesh displacement of the gear pair (mm)	0.115	0.084	26.96%
Maximum dynamic torque of motor shaft (Nm)	400	285	28.75%
Maximum dynamic torque of output shaft (Nm)	661	469	29.05%

that without ADCS, and the acceleration performance has hardly decreased. The mesh force and mesh displacement of IEDS gear pair are shown in Figure 28. During acceleration, the maximum mesh force decreases from 1.72×10^4N to 1.32×10^4N, and the maximum mesh displacement decreases from 0.115mm to 0.084mm. Figure 29 (a) and Figure 29(b) show the dynamic torque transmitted by the motor shaft and output shaft respectively. The maximum dynamic torque of motor shaft decreases from 400Nm to 285Nm, and the maximum dynamic torque of output shaft decreases from 661Nm to 469Nm. The simulation results of the maximum dynamic load and deformation of IEDS mechanical system are summarized in Table 8. With almost no loss of acceleration performance, the ADCS proposed in this paper could effectively reduce the torsional vibration of IEDS during rapid acceleration, which can effectively improve the driving comfort and extend the life of IEDS.

V. CONCLUSION

In this paper, an electromechanical coupling model of the EV equipped with the integrated electric drive system is established including the motor model and the driveline dynamic model. The electromechanical dynamic response characteristics of the IEDS under the conditions of rapid acceleration and impact load are simulated and analyzed. Then, an active damping control strategy is proposed to suppress the torsional vibration of driveline during vehicle launch. The following two points should be noted:

1. During rapid acceleration, the sudden step torque produced by SPMSM excites violent torsional vibration of driveline, lead to the speed fluctuation and dynamic load increase of IEDS gear pair and shafts. In speed control mode, the SPMSM generates fluctuating torque which can effectively suppress the torsional vibration of driveline excited by the impact load applied to wheel.

2. ADCS is proposed to suppress the torsional vibration of driveline during vehicle launch. With the effect of ADCS, the maximum mesh force and displacement of the gear pair have reduced by 23.26% and 26.96% respectively, the maximum dynamic load of motor shaft and IEDS output shaft have reduced by 28.75% and 29.05% respectively. The simulation results indicate that ADCS could effectively suppress the

$$\boldsymbol{\theta} = \begin{bmatrix} \theta_m & \theta_1 & \theta_2 & \theta_g & \theta_w & \theta_v \end{bmatrix}^{\mathrm{T}};$$

$$\mathbf{T} = \begin{bmatrix} T_m & (k_m e + c_m \dot{e})R_p & -(k_m e + c_m \dot{e})R_g & \theta_g & \theta_w & \theta_v \end{bmatrix}^{\mathrm{T}};$$

$$\mathbf{M} = \begin{bmatrix} I_m & 0 & 0 & 0 & 0 & 0 \\ 0 & I_1 & 0 & 0 & 0 & 0 \\ 0 & 0 & I_2 & 0 & 0 & 0 \\ 0 & 0 & 0 & I_g & 0 & 0 \\ 0 & 0 & 0 & 0 & I_w & 0 \\ 0 & 0 & 0 & 0 & 0 & I_v \end{bmatrix};$$

$$\mathbf{C} = \begin{bmatrix} c_{s1} & -c_{s1} & 0 & 0 & 0 & 0 \\ -c_{s1} & c_{s1} + c_m \cdot R_p^2 & -c_m \cdot R_p \cdot R_g & 0 & 0 & 0 \\ 0 & -c_m \cdot R_p \cdot R_g & c_{s2} + c_m \cdot R_g^2 & -c_{s2} & 0 & 0 \\ 0 & 0 & -c_{s2} & c_{s2} + 2c_a/i_0^2 & -2c_a/i_0 & 0 \\ 0 & 0 & 0 & -c_a/i_0 & c_a + c_w & -c_w \\ 0 & 0 & 0 & 0 & -2c_w & 2c_w \end{bmatrix};$$

$$\mathbf{K} = \begin{bmatrix} k_{s1} & -k_{s1} & 0 & 0 & 0 & 0 \\ -k_{s1} & k_{s1} + k_m \cdot R_p^2 & -k_m \cdot R_p \cdot R_g & 0 & 0 & 0 \\ 0 & -k_m \cdot R_p \cdot R_g & k_{s2} + k_m \cdot R_g^2 & -k_{s2} & 0 & 0 \\ 0 & 0 & -k_{s2} & k_{s2} + 2k_a/i_0^2 & -2k_a/i_0 & 0 \\ 0 & 0 & 0 & -k_a/i_0 & k_a + k_w & -k_w \\ 0 & 0 & 0 & 0 & -2k_w & 2k_w \end{bmatrix}$$

$$G(s)$$
$$= \frac{(s+7143+37426i)(s+7143-37426i)(s+1851+15820i)(s+1851-15820i)(s+126+3084i)(s+126-3084i)(s+15+116i)(s+15-116i)(s+6i)(s-6i)}{s(s+7156+37428i)(s+7156-37428i)(s+1860+15844i)(s+1860-15844i)(s+128+3228i)(s+128-3228i)(s+15+142i)(s+15-142i)(s+4+47i)(s+4-47i)}$$

$$K(s)$$
$$= \frac{(s+7143+37426i)(s+7143-37426i)(s+1851+15820i)(s+1851-15820i)(s+126+30841i)(s+126-30841i)(s+15+116i)(s+15-116i)(s+6i)(s-6i)}{(s+7156+37428)(s+7156-374281)(s+1860+158441)(s+1860-158441)(s+128+3228i)(s+128-3228i)(s+15+142)(s+15-142i)(s+4+47i)(s+4-47i)}$$

$$f(s) = \frac{(s+143)^3(s+48)^3(s+7143+37426i)(s+7143-37426i)(s+1851+15820i)}{(s+1851-15820i)(s+126+3084i)(s+126-3084i)(s+15+116i)(s+15-116i)(s+6i)(s-6i)}{(s+28)(s+81)(s+7156+37428i)(s+7156-37428i)(s+1860+15844i)(s+1860-15844i)(s+178+145i)(s+178-145i)(s+128-3229i)}{(s+128-3229i)(s+50+33i)(s+50-33i)(s+21+137i)(s+21-137i)(s+4+43i)(s+4-43i)}$$

torsional vibration of driveline with almost no loss of acceleration performance. Thus, the ADCS proposed in this paper can further extend the life of IEDS and improve the vehicle driving comfort without additional mechanical components.

APPENDIXES
APPENDIX I
Matrixes **M, C, K, θ** and **T** stated in Equation (19), as shown at the bottom of the previous page.

APPENDIX II
The transfer function $G(s)$, $K(s)$ and $F(s)$, as shown at the top of this page.

REFERENCES

[1] D. Q. Dang, M. S. Rafaq, H. H. Choi, and J.-W. Jung, "Online parameter estimation technique for adaptive control applications of interior PM synchronous motor drives," *IEEE Trans. Ind. Electron.*, vol. 63, no. 3, pp. 1438–1449, Mar. 2016.

[2] H. Wang, S. Li, J. Yang, and X. Zhou, "Continuous sliding mode control for permanent magnet synchronous motor speed regulation systems under time-varying disturbances," *J. Power Electron.*, vol. 16, no. 4, pp. 1324–1335, 2016.

[3] E. W. Zurita-Bustamante, H. Sira-Ramirez, J. Linares-Flores, O. D. Ramírez-Cárdenas, M. A. Contreras-Ordaz, and J. F. Guerrero-Castellanos, "On the active disturbance rejection control of the permanent magnet synchronous motor," in *Proc. IEEE Power Energy Conf. Illinois (PECI)*, Feb. 2018, pp. 1–6.

[4] M. Dogan and M. Dursun, "Application of speed control of permanent magnet synchronous machine with PID and fuzzy logic controller," *Energy Edu. Sci. Technol. A, Energy Sci. Res.*, vol. 28, no. 2, pp. 925–930, 2012.

[5] C. Zhou, D. C. Quach, N. Xiong, S. Huang, Q. Zhang, Q. Yin, and A. V. Vasilakos, "An improved direct adaptive fuzzy controller of an uncertain PMSM for Web-based E-service systems," *IEEE Trans. Fuzzy Syst.*, vol. 23, no. 1, pp. 58–71, Feb. 2015.

[6] S. Li, H. Won, X. Fu, M. Fairbank, D. C. Wunsch, and E. Alonso, "Neural-network vector controller for permanent-magnet synchronous motor drives: Simulated and hardware-validated results," *IEEE Trans. Cybern.*, to be published.

[7] R. Errouissi, M. Ouhrouche, W.-H. Chen, and A. M. Trzynadlowski, "Robust cascaded nonlinear predictive control of a permanent magnet synchronous motor with antiwindup compensator," *IEEE Trans. Ind. Electron.*, vol. 59, no. 8, pp. 3078–3088, Aug. 2012.

[8] R. Guo, C. Cao, Y. Mi, and Y. Huang, "Experimental investigation of the noise, vibration and harshness performances of a range-extended electric vehicle," *Proc. Inst. Mech. Eng. D, J. Automobile Eng.*, vol. 230, no. 5, pp. 650–663, 2016.

[9] R. Guo, H. Chen, and M.-J. Wang, "Modeling and active control of power-split hybrid electric vehicle launch vibration," *J. Low Freq. Noise, Vib. Active Control*, vol. 38, no. 2, pp. 592–607, 2019.

[10] L. Zhang, P. Zheng, D. Meng, Z. Z. Zhang, and H. Deng, "Experimental study and control of longitudinal flutter during vehicle starting with motor drive mode for hybrid electric car," *Automot. Eng.*, vol. 35, no. 3, pp. 212–218, 2013.

[11] T. Karikomi, K. Itou, T. Okubo, and S. Fujimoto, "Development of the shaking vibration control for electric vehicles," in *Proc. IEEE SICE-ICASE Int. Joint Conf.*, Oct. 2006, pp. 2434–2439.

[12] Z. Zhao, C. Wang, T. Zhang, and M. Li, "Anti-shake control with feedforward correction and active damping control in tip-in/out phases of pure electric driving," *Automot. Eng.*, vol. 40, no. 1, pp. 19–27 and 75, 2018.

[13] Y. Sato, S. Ishikawa, T. Okubo, M. Abe, and K. Tamai, "Development of high response motor and inverter system for the Nissan LEAF electric vehicle," SAE Tech. Paper 2011-01-0350, 2011.

[14] T. Yoo, H. Park, G. Kang, and S. Lim, "Development of vibration suppression control strategy for motor system of eco-friendly vehicles," SAE Tech. Paper 2014-01-1874, 2014.

[15] Q. Wang, K. Rajashekara, Y. Jia, and J. Sun, "A real-time vibration suppression strategy in electric vehicles," *IEEE Trans. Veh. Technol.*, vol. 66, no. 9, pp. 7722–7729, Sep. 2017.

[16] R. Guo and M.-J. Wang, "Active control of hybrid electric vehicle launch vibration in pure electric mode," *J. Vib. Control*, vol. 24, no. 4, pp. 673–681, 2018.

[17] Z. Song, J. Li, Z. Shuai, L. Xu, and M. Ouyang, "Fuzzy logic torque control system in four-wheel-drive electric vehicles for active damping vibration control," *Int. J. Vehicle Des.*, vol. 68, pp. 55–80, Jan. 2015.

[18] H. Fu, C. Feng, and S. Xue, "Vibration suppression control of an integrated powertrain of electric and hybrid vehicles using LQR controller and reduced-order observer," in *Proc. IEEE Conf. Expo Transp. Electrific. Asia–Pacific (ITEC Asia–Pacific)*, Aug./Sep. 2014, pp. 1–6.

[19] K. Szabat and T. Orlowska-Kowalska, "Vibration suppression in a two-mass drive system using pi speed controller and additional feedbacks—Comparative study," *IEEE Trans. Ind. Electron.*, vol. 54, no. 2, pp. 1193–1206, Aug. 2007.

[20] A. F. Boz and Y. Sari, "Generalized optimal controller design for all pole systems using standard forms," *Sci. Res. Essays*, vol. 4, no. 3, pp. 167–174, 2009.

[21] P. Shi, B. Liu, and D. Hou, "Torsional vibration suppression of drive system based on DMC method," in *Proc. IEEE 7th World Congr. Intell. Control Automat.*, Jun. 2008, pp. 4789–4792.

[22] Z. Ren, J. Xie, S. Zhou, and B. Wen, "Vibration characteristic analysis of helical gear-rotor-bearing system with coupled lateral-torsional-axial," *J. Mech. Eng.*, vol. 51, no. 15, pp. 75–89, 2015.

[23] F. Wang, Z.-D. Fang, and S.-J. Li, "Treatment and contrast verification of meshing stiffness in dynamic model of helical gear," *J. Vib. Shock*, vol. 33, no. 6, pp. 13–17, 2014.

[24] Y.-J. Wu, Y. Liang, Y. Yang, and J.-J. Wang, "Dynamic meshing characteristics of a gear pair using contact finite element method," *J. Vib. Shock*, vol. 31, no. 19, pp. 61–67, 2012.

[25] A. Kahraman, A. A. Kharazi, and M. Umrani, "A deformable body dynamic analysis of planetary gears with thin rims," *J. Sound Vib.*, vol. 262, no. 3, pp. 752–768, 2003.

[26] A. Kahraman, H. Ligata, and A. Singh, "Influence of ring gear rim thickness on planetary gear set behavior," *J. Mech. Des.*, vol. 132, no. 2, 2010, Art. no. 021002.

[27] G. Sika and P. Velex, "Instability analysis in oscillators with velocity-modulated time-varying stiffness—Applications to gears submitted to engine speed fluctuations," *J. Sound Vib.*, vol. 318, nos. 1–2, pp. 166–175, 2008.

[28] C. Liu, D. Qin, T. C. Lim, and Y. Liao, "Dynamic characteristics of the herringbone planetary gear set during the variable speed process," *J. Sound Vib.*, vol. 333, no. 24, pp. 6498–6515, 2014.

[29] C. Liu, D.-T. Qin, and Y. H. Liao, "Dynamic model for a parallel-axis helical gears transmission system based on variable friction coefficient between contact teeth," *J. Vib. Shock*, vol. 33, no. 24, pp. 150–157, 2014.

[30] Y. Yi, D. Qin, and C. Liu, "Investigation of electromechanical coupling vibration characteristics of an electric drive multistage gear system," *Mech. Mach. Theory*, vol. 121, pp. 446–459, Mar. 2018.

[31] G. Mandic, A. Nasiri, E. Muljadi, and F. Oyague, "Active torque control for gearbox load reduction in a variable-speed wind turbine," *IEEE Trans. Ind. Appl.*, vol. 48, no. 6, pp. 2424–2432, Nov./Dec. 2012.

[32] J. Licari, C. E. Ugalde-Loo, J. B. Ekanayake, and N. Jenkins, "Comparison of the performance and stability of two torsional vibration dampers for variable-speed wind turbines," *Wind Energy*, vol. 18, no. 9, pp. 1545–1559, 2015.

MEIXIA JIA received the B.S. and M.S. degrees from Jilin University at Changchun, Jilin, China. She is currently pursuing the Ph.D. degree in vehicle engineering with Chongqing University. Her research interests include vehicle control and the multiphysical field coupling of motor used in electric vehicle.

JIANJUN HU received the B.S., M.S., and Ph.D. degrees in automotive engineering from Chongqing University, Chongqing, China. He is also a Researcher with the State Key Laboratory of Mechanical Transmission. His research interests include vehicle power transmission, hybrid electric vehicle control, and motor control used for electric vehicle.

YING YANG received the B.Eng. degree in automotive engineering from Chongqing University, in 2018, where he is currently pursuing the master's degree in automotive engineering. His research interests include motor control and multiphysical field simulation.

TAO PENG received the B.Eng. degree in automotive engineering from Xihua University, in 2017. He is currently pursuing the master's degree in automotive engineering with Chongqing University. His research interests include motor control and hybrid electric vehicle energy management strategy.

YONGJIE GUAN received the B.Eng. degree in vehicle engineering from Chongqing University, in 2018, where he is currently pursuing the master's degree in vehicle engineering. His research interest includes control and analysis of electrical motors.

• • •